

1 **Iron-modulated Nickel Cobalt Phosphide Embedded in Carbon to Boost Power**  
2 **Density of Hybrid Sodium–air Battery**

3 Yao Kang<sup>a,#</sup>, Shuo Wang<sup>a,#</sup>, Siqi Zhu<sup>a,#</sup>, Haixing Gao<sup>a</sup>, Kwan San Hui<sup>b,\*</sup>, Feng Bin<sup>c</sup>,  
4 Xi-Lin Wu<sup>d</sup>, Wenjie Mai<sup>e</sup>, Ling Zhu<sup>f</sup>, Feng Liang<sup>g,\*</sup>, Fuming Chen<sup>h,\*</sup>, Kwun Nam  
5 Hui<sup>a,\*</sup>

6 <sup>a</sup> Joint Key Laboratory of the Ministry of Education, Institute of Applied Physics and  
7 Materials Engineering, Universit of Macau, Avenida da Universidade, Taipa, Macau  
8 SAR, China

9 <sup>b</sup> Engineering, Faculty of Science, University of East Anglia, Norwich, NR4 7TJ,  
10 United Kingdom

11 <sup>c</sup> State Key Laboratory of High-Temperature Gas Dynamics, Institute of Mechanics,  
12 Chinese Academy of Science, Beijing 100190, PR China

13 <sup>d</sup> College of Geography and Environmental Science, Zhejiang Normal University,  
14 Jinhua, 321004, China

15 <sup>e</sup> Siyuan Laboratory, Guangdong Provincial Engineering Technology Research Center  
16 of Vacuum Coating Technologies and New Energy Materials, Department of Physics,  
17 Jinan University, Guangzhou 510632, People's Republic of China.

18 <sup>f</sup> College of Physics and Optoelectronics Engineering, Shenzhen University, Nanhai  
19 Ave, 3688, Shenzhen, Guangdong 518060, China

20 <sup>g</sup> State Key Laboratory of Complex Nonferrous Metal Resources Clean Utilization,  
21 Kunming University of Science and Technology, Kunming 650093, China

22 <sup>h</sup> School of Physics and Telecommunication Engineering, South China Normal  
23 University, Guangzhou 510006, P.R. China.

24 <sup>#</sup> These authors contributed equally

25 <sup>\*</sup> Corresponding author

26 Kwan San Hui, E-mail: k.hui@uea.ac.uk

27 F. Liang, E-mail: liangfeng@kust.edu.cn

28 Fuming Chen, E-mail: fmchen@m.scnu.edu.cn

29 Kwun Nam Hui, E-mail: bizhui@um.edu.mo

30

31

32

33 **Abstract**

1 Nickel cobalt phosphide (NiCoP) is emerging as a potential electrocatalyst towards  
2 oxygen reduction reaction (ORR) and oxygen evolution reaction (OER). However, its  
3 ORR/OER activities are sluggish. Here, we investigated the roles of iron dopants in the  
4 Fe-doped NiCoP (Fe–NiCoP) in order to boost its ORR/OER kinetics. The density  
5 functional theory calculations reveal that the Fe dopant effectively modulates the  
6 electron conductivity of the Fe–NiCoP and reduces binding energies of the reaction  
7 intermediates towards rate-determining steps of ORR and OER. A binder-free 3D  
8 microflowers morphology of the Fe–NiCoP embedded in the amorphous carbon layer  
9 (Fe–NiCoP@C) catalyst on the nickel foam was prepared as the air cathode for the  
10 hybrid Na-air battery (HSAB). The HSAB displays a discharge voltage of 2.74 V at  
11  $0.01 \text{ mA cm}^{-2}$  with excellent round trip efficiency of 93.26% at the 500<sup>th</sup> cycle and  
12 state-of-the-art power density of  $621 \text{ mW g}^{-1}$ .

13

14

15

16

17

18

19

20 **Keywords:** *Iron doping, nickel cobalt phosphide, electronic structure reformation, DFT*  
21 *calculation, hybrid sodium-air battery*

22 **1. Introduction**

1 The rapid development of electric vehicles has stimulated the large demand for high-  
2 performance energy conversion and storage technologies, tackling the critical problems  
3 of climate change and energy crisis. Rechargeable metal–air batteries, especially,  
4 hybrid sodium-air batteries (HSABs) have attracted increasing attention due to their  
5 high theoretical energy density ( $2600 \text{ Wh kg}^{-1}$ ), natural abundance, and  
6 environmentally friendly characteristics [1-5]. In 2016, we are the first to show that the  
7 HSAB exhibits a large specific capacity of  $835 \text{ mAh g}^{-1}$  at  $50 \text{ }^\circ\text{C}$  (corresponding to 99%  
8 of the theoretical capacity) [2]. However, the practical application of HSABs has been  
9 largely obstructed by the four proton–electron transfer kinetics of oxygen reduction  
10 reaction (ORR) and oxygen evolution reaction (OER) due to the thermodynamically  
11 unfavorable process with large overpotential [1, 6]. Although noble metals, such as  
12 platinum (Pt) and ruthenium (Ru) or iridium (Ir), have been commonly regarded as  
13 efficient electrocatalysts in ORR and OER, the high cost, scarcity, and poor chemical  
14 stability of these noble metal-based electrocatalysts have hindered their large-scale  
15 applications in HSABs [7, 8]. Thus, the successful development of low-cost and highly  
16 efficient bifunctional electrocatalysts towards ORR and OER for HSABs has a  
17 significant impact on realizing the net-zero carbon society.

18

19 Recently, transition metal phosphides (TMPs), such as  $\text{Co}_2\text{P}$  [9, 10],  $\text{CoP}$  [11],  $\text{Ni}_2\text{P}$   
20 [12], and  $\text{MoP}$  [13, 14], have been recognized as promising alternatives to noble metal-  
21 free catalysts for the trifunctional electrocatalysts of ORR, OER, and hydrogen  
22 evolution reaction due to their multielectron orbitals, metallic characteristics, and low

1 cost. Among these TMPs, NiCoP is particularly attractive because of two  
2 electrochemically feasible transition metals such as Ni and Co that contribute to the  
3 ORR and OER [15-18]. However, the critical problem of sluggish ORR/OER kinetics  
4 remains unaddressed, that is caused by the strong binding strength of the absorbed  
5 intermediates with the surface of Co and Ni atoms [15-18]. According to the Sabatier  
6 principle, the best catalysts should bond atoms or molecules with an intermediate  
7 strength: too weak interaction is not conducive to the activation of reactants, and too  
8 strong interaction is not beneficial for the desorption of products [19]. Therefore, there  
9 is a pressing need to improve our understanding of how to tune the  
10 adsorption/desorption strength of intermediates at the active sites of NiCoP, facilitating  
11 the ORR/OER kinetics and hence advancing metal-air batteries for large-scale  
12 applications.

13

14 In this study, through combined density functional theory (DFT) calculations and  
15 experimental investigations, we aim to understand the influence of Fe dopant in Fe-  
16 doped NiCoP (Fe-NiCoP) towards ORR/OER, in order to unveil its roles and the origin  
17 of improved ORR/OER activities. In addition, a layer of carbon coating is further coated  
18 onto the Fe-NiCoP surface (Fe-NiCoP@C) to facilitate the electron transport to and  
19 from the catalytic sites and further improve its catalytic performance and stability in  
20 the ORR and OER. The DFT calculations reveal that the Fe dopants in the Fe-NiCoP  
21 are the active sites for ORR/OER activities. The improved ORR/OER kinetics are  
22 facilitated by the enhanced electronic property of Fe-NiCoP@C and the reduced free

1 energies of adsorption of oxygen-containing intermediates. The Fe–NiCoP@C catalyst  
2 exhibits excellent electrocatalytic performance toward ORR and OER with an onset  
3 potential of 0.81 V and exceptional overpotential of 340 mV at a current density of 50  
4 mA cm<sup>-2</sup>, which are higher than most of the non-noble metal-based ORR and OER  
5 catalysts reported to date. A HSAB, utilizing the binder-free 3D microflowers  
6 morphology of the Fe–NiCoP@C catalyst on the nickel foam as the air cathode,  
7 displays a discharge voltage of 2.74 V at 0.01 mA cm<sup>-2</sup> with excellent round trip  
8 efficiency of 93.26% at the 500<sup>th</sup> cycle and the state-of-the-art power density of 621  
9 mW g<sup>-1</sup>. The new understanding from this study helps to design new TMPs catalysts  
10 for advancements of metal-air batteries, realizing the potential of electric vehicles.

11

## 12 **2. Experimental**

13 **2.1. Synthesis of Fe–NiCo LDH.** The Fe-NiCo LDH were prepared by hydrothermal  
14 methods. Specifically, Nickel foam (NF) were cleaned with the assistance of sonication  
15 in HCl, ethanol, and water for 10 min each. Then, Ni(NO<sub>3</sub>)<sub>2</sub>·6H<sub>2</sub>O, Fe(NO<sub>3</sub>)<sub>3</sub>·9H<sub>2</sub>O,  
16 and Co(NO<sub>3</sub>)<sub>2</sub>·6H<sub>2</sub>O (2:1:1) with 4 mmol NH<sub>4</sub>F and 10 mmol urea were dissolved in  
17 40 mL deionized (DI) water. Then, NF (2\*3) and the solution were transferred into a 50  
18 mL Teflon autoclave, sealed, and maintained at 120 °C for 9 h. The specific activity of  
19 the material for the target reaction is usually highly dependent on the chemical  
20 composition and their electronic structures. It has been demonstrated that Ni usually  
21 have a great influence on the OER activities, while Co and Fe ions are believed to be  
22 the active center towards ORR with specific crystal and electronic structures. To ensure

1 the bifunctional catalytic performance of Fe-NiCoP for hybrid sodium-air battery, the  
2 ratio of Ni:Co and Ni:Co:Fe are about 1:1 and 1:0.5:0.5 for NiCoP and Fe-NiCoP,  
3 respectively.

4 **2.2. Synthesis of Fe-NiCoP.** To prepare the Fe-NiCoP@NF, the obtained Fe-NiCo  
5 LDH and 2 g NaH<sub>2</sub>PO<sub>2</sub>·H<sub>2</sub>O were placed in two ceramic boats inside a tube furnace  
6 and annealed 300 °C for 2 h in a static N<sub>2</sub> atmosphere. Then, the samples were naturally  
7 cooled to room temperature in N<sub>2</sub> atmosphere.

8 **2.3. Synthesis of Fe-NiCoP@C.** The leaching of anions from layered double  
9 hydroxides during oxidative reactions is still an important issue. Therefore, a layer of  
10 carbon was coated onto the Fe-NiCoP surface to stabilize the catalyst-electrolyte  
11 interface and provide additional direct electron transport paths. In the fabrication of  
12 carbon shell on the obtained Fe-NiCoP microflowers, the sample was transferred to a  
13 Teflon autoclave with 40 mL glucose solution (0.15 M) and then maintained at 180 °C  
14 for 4 h in an oven. Finally, the sample was carbonized at 400 °C for 2 h with an  
15 accelerating rate of 5 °C/min in N<sub>2</sub> atmosphere.

16 **2.4. Electrochemical measurement.** The electrochemical performance was carried out  
17 in a three-electrode setup with a CHI760e electrochemical station. Herein, Fe-  
18 NiCoP@C, Fe-NiCoP, NiCoP, commercial Pt/C, and Ir/C was utilized as the working  
19 electrode, Ag/AgCl and Pt foil was used as reference electrode and counter electrode,  
20 respectively. In this study, all potentials were calibrated to the reversible hydrogen  
21 electrode (RHE):  $E_{RHE} = E_{measured} + 0.059 \cdot pH + 0.197$  V. The OER performance was  
22 tested in 1 M KOH without iR-correction. To investigate the ORR performance of

1 materials, the active materials were peeled from the NF. 10 mg catalysts were added  
2 into 980  $\mu\text{l}$  ethanol with 20  $\mu\text{l}$  of 5wt % Nafion solution to make catalyst ink. To prepare  
3 working electrode, 40  $\mu\text{l}$  catalyst ink was dropped onto the surface of glass carbon  
4 electrode (diameter: 5mm). The ORR performance of electrode was recorded in 0.1 M  
5 KOH at 1600 rpm with a sweep rate of 10  $\text{mV s}^{-1}$ . All fresh electrolytes were bubbled  
6 with nitrogen for 30 min before test.

7 **2.5. Assembly of the HSAB.** The liquid anode was prepared by dissolving sodium  
8 metal into a solution of tetra ethylene glycol dimethyl ether. A piece of NASICON  
9 composed of  $\text{Na}_3\text{Zr}_2\text{Si}_2\text{PO}_{12}$  with high ionic conductivity of  $1.0 \times 10^{-3} \text{ S cm}^{-1}$  at room  
10 temperature was used as the separator [20, 21]. The oxygen-saturated 0.1 M NaOH  
11 solution, which was used as the aqueous electrolyte, was sealed in a tube. A porous  
12 electrode containing  $0.12 \text{ mg cm}^{-2}$  catalyst was utilized as the air electrode. HSABs  
13 were assembled in a glove box filled with high-purity argon ( $\text{O}_2$  and  $\text{H}_2\text{O} < 0.1 \text{ ppm}$ )  
14 according to the following structure: liquid anode | NASICON | catholyte | catalytic  
15 cathode. The electrochemical performance of HSAB was tested at room temperature.

## 16 **2.6. Material characterization**

17 The crystallographic structure was determined using a Rigaku SmartLab XRD  
18 equipped with Cu  $K\alpha$  radiation ( $\lambda = \sim 1.54 \text{ \AA}$ ), and the data were collected in the Bragg–  
19 Brentano mode with a scan rate of  $5^\circ \text{ s}^{-1}$ . The morphology and structure were  
20 characterized using a Zeiss Sigma field emission scanning and Talos F200S  
21 transmission electron microscopes with an EDS probe. The surface chemical states  
22 were analyzed using a Thermo Scientific ESCALAB Xi<sup>+</sup> XPS Microprobe with Al- $K\alpha$

1 radiation. ICP-AES (Thermo Jarrell Ash) was used to indicate the elemental  
2 composition of materials.

### 3 **2.7. Computational Details**

4 All the calculations based on DFT were performed using the Vienna ab-initio  
5 Simulation Package in order to optimize the geometry structures and energies [22, 23].

6 The exchange–correlation interactions of the generalized gradient approximation were  
7 determined in the scheme of Perdew–Burke–Ernzerhof functional [24, 25]. The core  
8 electrons was described using the Projector Augmented Wave (PAW) potential [26].

9 The cut-off kinetic energies in the plane waves were set to 450 eV for all the calculations.

10 The convergence tolerance of energy and force on each atom during structure relaxation  
11 were less than  $10^{-4}$  eV and  $0.02$  eV/Å<sup>o</sup>, respectively. We build the 112 supercell of bulk  
12 Co<sub>2</sub>P ( $a=b=5.73$  Å,  $c=3.41$  Å;  $\alpha=\beta=90^\circ$ ,  $\gamma=120^\circ$ ) to dope Ni and Co atoms and ensure  
13 that the doping ratio is consistent with the experiment results (Fe:Co:Ni = 1:1:2 (at%) ).

14 Then, the cleave surface (111) of NiCoP and Fe-NiCoP are used for the subsequent  
15 adsorption calculation. The pseudo-potentials of Fe, Co and Ni metals all use the

16 pseudo-potentials recommended by the VASP official website. We set the Brillouin  
17 zone with a Gamma-centered k-point grid of  $5 \times 5 \times 1$ , and a vacuum space of around

18  $20$  Å was set along the z direction to avoid the interaction between periodical images  
19 [27]. Moreover, Grimme’s DFT-D3 scheme was used to perform dispersion correction

20 and describe the van der Waals (vdW) interactions in the systems [28, 29]. The

21 Hubbard-U correction method was applied to improve the descriptions of the strong

22 localized Ni, Co, and Fe d-electrons in Fe–NiCoP with  $U = 5.3$ ,  $U = 3.32$  and  $U = 6.45$



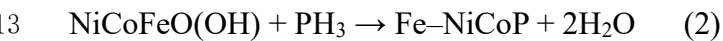
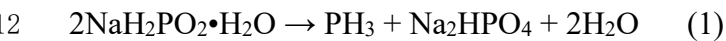
1 for Fe, Co, and Ni, respectively. These values were taken from previous studies. Spin  
2 polarization was also considered in all the calculations.

3

### 4 **3. Results and discussion**

#### 5 **3.1. Synthesis of Fe-NiCoP@C**

6 The synthetic route of Fe-NiCoP@C composites is presented in Fig. 1a. Specifically, a  
7 hydrothermal method was initially applied, after which a yellow film was observed on  
8 the surface of the Ni foam, thus implying the successful formation of iron nickel cobalt  
9 layered double hydroxide (Fe-NiCo LDH) [30]. The obtained Fe-NiCo LDH precursor  
10 was subsequently converted to Fe-NiCoP via low-temperature phosphorization by  
11 using  $\text{NaH}_2\text{PO}_2$  as the P source [31, 32].



14 After phosphorization, a carbon layer was coated onto the hierarchical Fe-NiCoP via  
15 hydrothermal carbonization of glucose [33]. During the process, glucose molecules  
16 were first cross-linked through the dehydration process to form an organic network  
17 surrounding the entire hierarchical Fe-NiCoP structure [33]. Finally, Fe-NiCoP@C  
18 was formed by annealing the cross-linked organic network at 400 °C for 2 h under an  
19 argon atmosphere to form a carbonized layer with abundant oxygen functional groups  
20 [33].

21

#### 22 **3.2. Characterizations of materials**

1 The X-ray diffraction (XRD) patterns of NiCoP, Fe–NiCoP, and Fe–NiCoP@C are  
2 shown in Fig. 1b. Compared to the XRD patterns of Fe–NiCo LDH (Fig. S1), the  
3 diffraction peaks at  $41.0^\circ$ ,  $47.6^\circ$ , and  $54.5^\circ$  can be indexed to the (111), (210), and (211)  
4 crystal planes of NiCoP (JCPDS#71–2336), respectively, thereby indicating successful  
5 Fe incorporation without any phase change [34]. The scanning electron microscopy  
6 (SEM) results revealed that Fe–NiCo LDH, Fe–NiCoP, and Fe–NiCoP@C all exhibited  
7 a microflower-like morphology with the diameter ranging from 5  $\mu\text{m}$  to 7  $\mu\text{m}$ , as shown  
8 in Fig. 1c–1e, indicating that the morphology was not influenced by phosphorization  
9 and carbonization. In addition, the enlarged SEM images (Fig. S2) showed that the  
10 surface of Fe–NiCoP was rough, suggesting that abundant active sites were generated  
11 after phosphorization. These bumps might be created due to the different inward and  
12 outward diffusion rates of P and  $\text{OH}^-$  during the phosphorization process [35]. The  
13 detailed SEM images shown in Fig. 1e–1g and Fig. S2 showed that the Fe–NiCoP@C  
14 surface roughened considerably due to the integration of carbon networks in the Fe–  
15 NiCoP nanosheets. Firstly, the hierarchical carbon shell provides facile electron-  
16 transfer pathways between the active catalyst and the current collector. Secondly, the  
17 hierarchical structure also provides reactant/product exchange channels between  
18 neighboring chambers that are constructed by Fe–NiCoP@C nanosheet arrays.  
19 Transmission electron microscopy (TEM) was performed to gain further insights into  
20 the morphologies and sizes of the as-prepared materials. The Fe–NiCoP nanosheets  
21 clearly contained numerous bumps on the surface, which can provide extra  
22 electroactive sites and further boost their electrocatalytic performance (Fig. 2a and Fig.

1 S3). As shown in Fig. 2b, the carbon layer with an approximate thickness of 5-15 nm  
2 was coated on the surface of Fe–NiCoP, and this coating was beneficial to the efficient  
3 electron transfer to and from the electroactive sites of the catalyst. The high-resolution  
4 TEM (HRTEM) images (Fig. 2c) of a single nanosheet of Fe–NiCoP@C demonstrated  
5 appropriately resolved lattice fringe spacings of 0.262 and 0.219 nm, corresponding to  
6 the (211) and (111) planes of NiCoP, respectively. This finding was also supported by  
7 several bright discrete spots in the selected area electron diffraction (SAED) pattern  
8 (insert of Fig. 2c), which could be indexed to the (111), (210), and (211) planes of  
9 NiCoP. Meanwhile, Fig. 2d–2i show the high-angular annular dark field scanning TEM  
10 (HAADF–STEM); energy dispersive X-ray (EDX) mapping was then used to further  
11 investigate the element distribution of Fe–NiCoP@C. The EDX mapping in Fig. 2d–2i  
12 indicated the almost homogeneous distributions of Ni, Co, Fe, P, and C except two rich  
13 signal of Ni in the EDX mapping, this may be attributed to the Ni region that connected  
14 Ni foam.

15  
16 The surface chemical composition and atom valence states of NiCoP, Fe–NiCoP, and  
17 Fe–NiCoP@C were further examined by using X-ray photoelectron spectroscopy  
18 (XPS), as shown in Fig. 3. The XPS survey spectra identified the presence of Ni, Co,  
19 Fe, P, and C in the Fe–NiCoP@C electrode, suggesting the successful doping of Fe  
20 atoms and carbon coating. Specifically, the high-resolution XPS spectra of the Ni 2p,  
21 Co 2p, and Fe 2p regions of the catalysts were split into  $2p_{3/2}$  and  $2p_{1/2}$  doublets due to  
22 the spin–orbit coupling [36]. Fe–NiCoP@C exhibited five main peaks in the Ni 2p

1 region. Two fitted peaks had binding energies of 856.2 (Ni 2p<sub>3/2</sub>) and 874.1 (Ni 2p<sub>1/2</sub>)  
2 eV, which are related to Ni 2p<sub>1/2</sub> and Ni 2p<sub>3/2</sub>, whereas the peaks at 861.2 and 879.6 eV  
3 could be assigned to the satellite peaks of Ni 2p (Fig. 3a) [36-38]. Similarly, in the high-  
4 resolution Co 2p spectrum of Fe–NiCoP@C (Fig. 3b), the binding energies of 782.4  
5 and 798.2 eV in the high-resolution Co 2p spectra were due to 2p<sub>3/2</sub> and 2p<sub>1/2</sub>, whereas  
6 two peaks at 787.4 and 804.3 eV were assigned to the satellites of Co 2p, respectively  
7 [39, 40]. Compared with NiCoP, the binding energies of Ni 2p and Co 2p in Fe–NiCoP  
8 and Fe–NiCoP@C shifted to higher binding energy, indicating electron transfer from  
9 Ni and Co to P atoms due to the incorporation of Fe, as discussed in the density  
10 functional theory (DFT). The high-resolution Fe 2p spectrum (Fig. 3c) showed four  
11 peaks divided into 712.1 eV of Fe 2p<sub>3/2</sub> and 724.4 eV of Fe 2p<sub>1/2</sub> with a spin–energy  
12 separation of 12.3 eV. The absence of characteristic FeP peaks in the Fe 2p region  
13 suggested the successful Fe doping in NiCoP [38]. As shown in Fig. 3d, the P 2p  
14 spectrum of Fe–NiCoP obtained a binding energy of 129.5 eV in 2p<sub>3/2</sub>, thereby  
15 indicating the presence of an M–P bond, whereas the centered peaks at 132.8 and 133.5  
16 eV were assigned to the oxidized phosphorus species (M–PO) [41]. Compared with  
17 NiCoP, a negative shift simultaneously occurred in the P 2p<sub>3/2</sub> binding energy (129.5  
18 eV) of Fe–NiCoP and Fe–NiCoP@C, indicating an modification of the electronic  
19 structure upon incorporation of Fe atom, as discussed in the DFT [42]. In the high-  
20 resolution XPS spectrum of C 1s (Fig. S4), the binding energies of 283.4, 284.2, and  
21 286.0 eV were assigned to the sp<sup>2</sup>-hybridized carbon atoms (–C–C–), C=C, and C(O)O,  
22 respectively [33]. Notably, the functionals groups, such as C–O–C/C–OH, C=O and -

1 COOH were observed in the C 1s. Such oxygen functional groups in carbonized layer  
2 facilitate the adsorption of water molecules via hydrogen bonding with oxygen  
3 functional groups [43]. In addition, these oxygen functional groups also provide  
4 additional active sites for ORR/OER activity by altering the electronic modulation of  
5 the adjacent carbon, which promotes the ORR/OER processes [44-46].

6

### 7 **3.3. ORR and OER electrocatalysis**

8 To evaluate the ORR performance of the as-prepared catalysts, rotating disk electrode  
9 measurements in O<sub>2</sub>-saturated 0.1 KOH were carried out. As indicated by the CV curves  
10 in Fig. 4a and Fig. S5, Fe–NiCoP@C displayed a reduction peak at the potential of 0.65  
11 V, which is more positive than those of Fe–NiCoP (0.55 V), NiCoP (0.45 V), FeP@C  
12 (0.47 V), and Fe–NiP@C (0.45 V) suggesting the superior ORR catalytic performance  
13 of Fe–NiCoP@C. Meanwhile, the linear sweep voltammetry (LSV) was also  
14 investigated to reveal the ORR performance of the samples. Fig. 4b shows the LSV  
15 curves of Fe–NiCoP@C. Compared with Fe–NiCoP (0.80 V) and NiCoP (0.64 V), Fe–  
16 NiCoP@C obtained the maximum positive onset potential of 0.81 V. In addition, the  
17 larger limit current density of Fe–NiCoP and Fe–NiCoP@C indicated superior ORR  
18 performance compared with NiCoP. The LSV curves at different rotations were  
19 obtained to explore the electron transfer number ( $n$ ) of air electrodes (Fig. 4c). The  
20 calculated  $n$  values of Fe–NiCoP@C, Fe–NiCoP, and NiCoP air electrodes were 3.75,  
21 3.70, and 2.32, respectively. In the case of Fe–NiCoP@C, the calculated  $n$  value was  
22 almost similar to the  $4e^-$  transfer number in the Pt/C. The ORR stability of Fe–

1 NiCoP@C was also investigated in an O<sub>2</sub> saturated 0.1 KOH solution. The  
2 chronopotentiometry plots in Fig. S6 show the relative current remains 80 % after  
3 10000 s, indicating acceptable stability of materials during the ORR test.

4  
5 To investigate the effect of Fe incorporation and the coating of carbon layer on the OER  
6 catalytic activity of the Fe–NiCoP@C electrode, a series of electrochemical tests were  
7 carried out in 1 M KOH using the typical three-electrode system with a scan rate of 10  
8 mV s<sup>-1</sup> (Fig. 4d). Notably, Fe–NiCoP@C shows the best ORR activity, which need the  
9 lowest overpotential of 270 mV at the current density of 10 mA cm<sup>-2</sup> compared to Fe–  
10 NiCoP (287 mV), NiCoP (319 mV), and Ir/C (350 mV). To achieve a higher current  
11 density of 50 mA cm<sup>-2</sup>, Fe–NiCoP@C retained the lowest overpotential of 340 mV  
12 compared with Fe–NiCoP (370 mV), NiCoP (420 mV), and Ir/C (480 mV), revealing  
13 its high catalytic OER activities. The Tafel slopes (Fig. 4f) further revealed that Fe–  
14 NiCoP@C exhibited a smaller Tafel slope of 36 mV dec<sup>-1</sup> than Ir/C (96 mV cm<sup>-1</sup>),  
15 NiCoP (65 mV dec<sup>-1</sup>), and Fe–NiCoP (62 mV dec<sup>-1</sup>), signifying a superior OER  
16 performance of Fe–NiCoP@C. To further investigate the electrode reaction kinetics,  
17 electrochemical impedance spectroscopy was conducted. The equivalent circuit (inset  
18 of Fig. S7) comprised an electrolyte resistance ( $R_s$ ) in series with a parallel combination  
19 of a constant phase element and a charge transfer resistance ( $R_{ct}$ ). The Nyquist plot (Fig.  
20 S7) showed a smaller  $R_s$  of Fe–NiCoP@C (3.2  $\Omega$ ) than those of Fe–NiCoP (3.5  $\Omega$ ) and  
21 NiCoP (4.2  $\Omega$ ), indicating that the Fe–NiCoP@C electrode possesses a low internal and  
22 interfacial resistances between the Fe–NiCoP@C surface and the electrolyte.

1 Furthermore, Fe–NiCoP@C revealed a significantly smaller semicircle in the low-  
2 frequency region than the Fe–NiCoP and NiCoP electrodes, indicating its smaller  
3 charge transfer resistance and faster mass transfer kinetics during OER.  
4 Electrochemically active surface area (ECSA) is another important criterion for  
5 evaluating the active sites of catalysts wherein capacitance  $C_{dl}$  is determined via a  
6 simple CV test with different scan rates (10, 20, 30, 40, 50, and 60  $\text{mV s}^{-1}$ ). The CV  
7 curves of Fe–NiCoP and Fe–NiCoP@C (Fig. S8) and the calculated effective  $C_{dl}$  of  
8 ECSA (Fig. 4g) indicated that Fe–NiCoP@C possessed a significantly higher ECSA  
9 value of  $100.1 \text{ mF cm}^{-2}$  than Fe–NiCoP ( $40.0 \text{ mF cm}^{-2}$ ) and NiCoP ( $18.6 \text{ mF cm}^{-2}$ ).  
10 Thus, the incorporation of Fe and the coating of carbon layer led to the increase in  
11 abundant electroactive sites.

12  
13 To evaluate the performance of electrocatalysts, electrochemical durability is carried  
14 out. The LSV curve of Fe–NiCoP@C remained nearly identical to the original curve  
15 after 1000 cycling tests (Fig. 4h), suggesting its excellent durability during cycling. To  
16 evaluate the durability of Fe–NiCoP@C, the long-term operation of the Fe–NiCoP@C  
17 sample was tested at 100, 150, and 200  $\text{mA cm}^{-2}$  (Fig. 4i). The insignificant increase in  
18 measured potential indicated the good stability of Fe–NiCoP@C. The structural  
19 stability of Fe–NiCoP@C was also confirmed by the SEM results after long-term  
20 cycling test (Fig. S9). The SEM image of the cycled Fe–NiCoP@C revealed the good  
21 retention of porosity and uniformity in the microflowers. The observed stability can be  
22 partially attributed to the unique electrode structure, which provided good gas release

1 ability and avoided the structural collapse caused by gas accumulation [33]. The robust  
2 mechanical strength between the as-grown catalysts and Ni foam substrates also  
3 contributed to the remarkable stability of Fe–NiCoP@C [33, 47]. In addition, previous  
4 study has demonstrated that Fe–NiCoP would be oxidized during the process of OER,  
5 which also occurred in this work [34]. It is unavoidable to protect the oxidation process  
6 during OER even though carbon nanoflakes were utilized to protect the electrode.  
7 According to HRTEM results, the crystal lattices are disordered, implying that more  
8 and more amorphous structure of Fe–NiCoP have been formed along with the progress  
9 of OER. It is known that an amorphous structure has a lot of advantages to promote the  
10 process of OER. Furthermore, XPS was also tested to further explored the surface  
11 chemical composition and atom valence states after 1000 cycles of the OER test (Fig.  
12 S10). As show in the Fig. S10, the XPS survey spectra identified the presence of Ni,  
13 Co, Fe, P, O, and C in the Fe–NiCoP@C electrode. In particular, the Ni 2p spectrum  
14 shows that the Ni-P peak at a binding energy of 852.6 eV disappeared and the intensity  
15 of Ni-PO at about 856 eV was increased, indicating that the Ni-P on the surface of  
16 particles is oxidized. In the Co 2p region, the peaks for Co 2p after cycling are shifted  
17 toward lower binding energies compared with the original ones in Fe–NiCoP@C,  
18 which may imply the decrement of electron transfer, but it is not particularly noticeable.  
19 As for the Fe 2p, no significant change in the state of Fe atoms, suggesting that  
20 electrochemical test have not much influence on the Fe element. It is worth noting that  
21 the intensity of P 2p at about 129.9 eV was decreased and oxidized P species formed at  
22 about 134.4 eV, indicating the surface oxidation process occurred during the



1 electrochemical test. In O 1s XPS spectrum, much oxygen element was observed after  
2 test, the fitted two peaks at 529.6 and 532.1 eV are ascribed to metal oxide (M-O), and  
3 metal oxyhydroxides (M-OH), respectively, which indicates that phosphides are  
4 slightly oxidized to phosphate, and the M-OH and M-O were gradually produced during  
5 the OER process, signifying the stability improvement [34]. These results revealed that  
6 Fe–NiCoP@C possessed significant durability in 1 M KOH.

7

8 To evaluate the catalytic properties of the Fe–NiCoP@C in real-life applications, the  
9 ORR and OER cycling performances of Fe–NiCoP@C was investigated using three  
10 electrodes in 0.1 M NaOH (4 h per cycle). No significant degradation was observed  
11 during all 45 cycles (Fig. S11). Furthermore, XRD was performed to investigate the  
12 chemical composition after cycling, and the results indicated the absence of an extra  
13 peak (Fig. S12) and the high structural stability of Fe–NiCoP@C during cycling.  
14 Notably, the majority of catalysts tend to experience severe erosion at high  
15 concentrations of the alkaline solution [33]. Therefore, the coating of the carbon layer  
16 on the Fe–NiCoP surface can provide effective protection against erosion and  
17 significantly improve the structural stability and cycling performance of the air  
18 electrode by reducing the leaching of P element during alkaline OER.

19

#### 20 **3.4. Mechanistic study on ORR and OER of materials**

21 DFT calculations were performed to identify the origin of high catalytic performance  
22 and reveal the inherent relationship between the selective ORR/OER activity and

1 atomic structure. To express the effect of doping clearly, the calculation model ignored  
2 the role of the outer carbon layer. Fig. S13a shows the top view of the (111) surface of  
3 the NiCoP structure, in which six-coordinated Co and the adjacent six-coordinated Ni  
4 atoms were exposed to the surface. In addition, the change of Bader charge between  
5 NiCoP and Fe-NiCoP (Table S3) indicates that the electrons transfer from Co and Ni  
6 atoms to neighbor P after the incorporation of Fe, which is consistent with XPS results  
7 and proved the rationality of the structure. Notably, the relatively lower \*OH and O<sub>2</sub>  
8 adsorption energies in the Co active site (-0.14 and -1.34 eV) than those in the Ni site  
9 (0.46 and -0.46 eV) of NiCoP indicated the more favorable OER and ORR processes  
10 (Table S4). In the Fe-NiCoP structure (Fig. S13b), two different active sites, the Fe  
11 atom and its adjacent Ni atom, were considered in the simulation of the OER/ORR  
12 reaction due to the incorporation of Fe on the NiCoP surface. The slightly lower \*OH  
13 and O<sub>2</sub> adsorption energies at the Fe site (-0.25 and -1.73 eV) compared with the values  
14 at the Ni-top site (0.46 and -0.42 eV) of Fe-NiCoP suggested that the Fe active sites  
15 were beneficial to OER and ORR. Therefore, the Co- and Fe-top sites were the active  
16 sites of the OER reaction before and after the incorporation of Fe, respectively.

17

18 The free energy pathways of the OER and ORR processes were also investigated  
19 through the simulation of the adsorption energies of intermediates, as shown in Fig. 5a-  
20 5d. The adsorption behaviors of essential intermediates (including \*OH, \*O, and \*OOH)  
21 during the OER process were investigated on the surface, implying that both the Co  
22 (NiCoP) and Fe (Fe-NiCoP) sites were stable in the adsorption of OER intermediates

1 (Fig. 5a–5b). Fig. 5c shows the diagram of OER Gibbs free energy ( $\Delta G$ ) in the (111)  
2 surface of NiCoP and Fe–NiCoP with correlative intermediates at the different reaction  
3 steps. The free energy profiles of NiCoP and Fe–NiCoP revealed how the OER rate-  
4 determining step (RDS) reflected the formation of \*OOH. Moreover, the calculated  
5 corresponding theoretical overpotentials of 0.81 and 1.01 eV in Fe–NiCoP and NiCoP,  
6 respectively, suggested a favorable OER process in Fe–NiCoP. In the ORR process, the  
7 formation of the  $\text{OH}^-$  is the RDS (Fig. 5d). Furthermore,  $\Delta G$  was calculated to be  
8 equivalent to an overpotential of 0.18 and 0.30 eV in Fe–NiCoP and NiCoP, respectively,  
9 suggesting that the Fe dopant could enhance the adsorption strength of the \*OH and  $\text{O}_2$   
10 (g) intermediates on the surface of the NiCoP structure (Table S3), subsequently  
11 reducing the overpotential and promoting the ORR catalytic activity in the Fe–NiCoP  
12 catalyst.

13  
14 To further understand the origin of the enhanced OER and ORR catalytic activities, the  
15 adsorption energies of \*OH, \*O, and \*OOH in NiCoP and Fe–NiCoP were calculated.  
16 The lower adsorption energies of \*OH, \*O, and \*OOH obtained in Fe–NiCoP (–0.25,  
17 1.09, and 2.70 eV) compared with those of NiCoP (–0.14, 1.24, and 3.04 eV) (Table  
18 S3.) suggested the more favorable OER and ORR reactions in the Fe–doped NiCoP  
19 slab. Meanwhile, the adsorption energies of \*OH, \*O, and \*OOH also provided insights  
20 into the distinct chemical adsorption characteristics of the Fe–NiCoP surface. The  
21 differences in charge density showed that electron transfers occurred between the  
22 interface of adsorbates (\*OH, \*OOH, \*O) and the Fe–NiCoP substrate, which can be

1 considered suitable adsorption sites for the intermediates (Fig. S14). The charge transfer  
2 from the substrate to the adsorbate might lead to effective molecule activation which,  
3 in turn, can promote the subsequent O<sub>2</sub> evolution [48]. Therefore, the decreased  
4 overpotential demonstrates that the OER and ORR activities in the catalysts are  
5 enhanced after the incorporation of Fe, and this finding is consistent with the  
6 experimental results.

7  
8 To further understand the inherent electron variation in the enhanced catalytic  
9 performance upon Fe incorporation, the total and partial density of states (TDOS and  
10 PDOS) were calculated, as shown in Fig. S15. The TDOS and PDOS plots showed the  
11 valence bands of both the up- and downspin channels in NiCoP and Fe–NiCoP near the  
12 Fermi level and the metallic character of materials. Compared with NiCoP (Fig. S15),  
13 the relatively higher TDOS value of Fe–NiCoP at the Fermi level indicated the efficient  
14 modulation of electrical conductivity, which was induced by the Fe dopant atom.  
15 Furthermore, the corresponding *p*- and *d*-bands in OER and ORR were calculated to  
16 illustrate the electron-hybridized property of NiCoP and Fe–NiCoP (Fig. 5e). The *p*-  
17 and *d*-band centers are effective descriptors in evaluating the performance of OER and  
18 ORR, respectively [49-53]. Compared with NiCoP (–5.18 eV), the calculated *p*-band  
19 centers of Fe–NiCoP (–4.63 eV) shifted toward the Fermi level, which increases the  
20 binding strength of \*OH, \*O, and \*OOH on the surface sites and results in low reaction  
21 barrier of the RDS, thus improving OER performance. When the Fe atom was doped  
22 on the surface of NiCoP, the top valence band of Fe was able to efficiently transfer

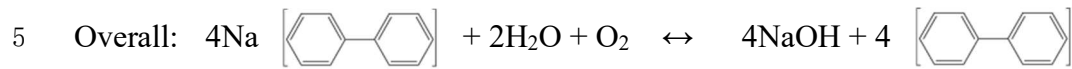
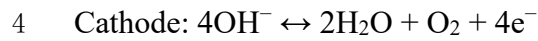
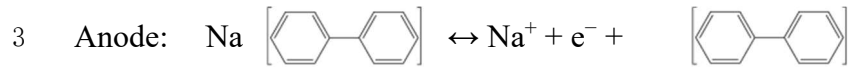
1 electrons to the P *p*-band of Fe–NiCoP, thus enhancing the M–P hybridization and OER  
2 performance [49]. In addition, previous studies have demonstrated that ORR activity is  
3 related to the *d*-band center of surface transition metals, which is correlated with the  
4 ability to form chemisorption bonds between oxygen intermediates and active sites. A  
5 distinct antibonding state appears above the Fermi level with the downshifting of the *d*-  
6 band center, and the stability of the chemisorption bond becomes increasingly strong  
7 with increasing numbers of antibonding states [51-53]. Our results (Fig. 5f) showed that  
8 the *d*-band center of all the metal atoms (Fe, Co, Ni) in Fe–NiCoP was shifted away  
9 from the Fermi level than that of pristine NiCoP, indicating the enhanced electronic  
10 interaction between the metals and P, and thus increasing the bonding strength between  
11 active sites and the oxygen intermediates. Hence, the increased catalytic activity  
12 observed in the Fe–NiCoP can be associated with the modified electronic properties  
13 induced by the incorporation of Fe dopant in NiCoP.

14

### 15 **3.5. Assembly of HSABs**

16 To evaluate the catalytic properties of Fe–NiCoP@C in real applications, HSABs were  
17 assembled consisting of a liquid anode, a NASICON solid electrolyte ( $\text{Na}_3\text{Zr}_2\text{Si}_2\text{PO}_{12}$ ),  
18 an aqueous catholyte, and an air electrode using Fe–NiCoP@C (Fig. 6a). During  
19 discharge, oxygen from the air diffused to the catalytic sites and then reduced to form  
20  $\text{OH}^-$ . Meanwhile, in the anolyte, the liquid anode was oxidized and  $\text{Na}^+$  was diffused  
21 with a NASICON solid electrolyte into the catholyte. Similarly, during the charge  
22 process,  $\text{Na}^+$  in the catholyte was transferred back to the anolyte through the NASICON

1 for electrodeposition on the anode. During the discharge–charge process, the reversible  
2 electrode and overall battery reactions occur as follows:



6 The electrochemical performance of fabricated HSABs was evaluated by examining  
7 their galvanostatic charge–discharge behaviors, as shown in Fig. 6b. In the figure,  $\Delta V$   
8 denotes the voltage gap between the charge and discharge voltages. The fabricated  
9 HSABs with Fe–NiCoP@C clearly showed the best battery performance with the  
10 lowest  $\Delta V$  of 0.14 V at the current density of  $0.01 \text{ mA cm}^{-2}$ , followed by the Fe–NiCoP  
11 (0.3 V) and NiCoP (0.83 V). The initial round trip efficiencies (the charge-to-discharge  
12 voltage ratio) of the HSABs were 95.1%, 90.1%, and 74.7% in Fe–NiCoP@C, Fe–  
13 NiCoP, and NiCoP, respectively. Fig. S16 shows the rate performance of HSAB with  
14 Fe–NiCoP@C electrode, an increased voltage gap was observed with increasing current  
15 density, which was attributed mainly to the high activation energy for the OER and  
16 ORR during battery operation at high current rates. Given that cycling performance and  
17 electrode stability are crucial to the air electrode in real applications, the constant  
18 current charge–discharge properties of HSABs were investigated for 500 cycles. Fig.  
19 6c shows the charge–discharge profiles of HSABs with the Fe–NiCoP@C air electrode.  
20 Notably, a slight fluctuation in charging-discharging gap in the initial cycling process  
21 was observed, which is attributed to the surface reconstruction of materials, however,  
22 no significant decrease in potential can be observed under the continuous charge–

1 discharge of batteries. To demonstrate the reversibility of the battery, the terminal  
2 discharge voltage and round trip efficiency of HSABs with the Fe–NiCoP@C electrode  
3 were measured (Fig. 6d). Notably, no significant degradation was observed after 500  
4 cycles and the round trip efficiency remained at 93.26%, thus revealing the high  
5 catalytic performance and excellent cycling performance of the Fe–NiCoP@C  
6 electrode. Compared with other reported materials in HSABs (Table S5), the  
7 remarkable fivefold enhancement in our results signified the excellence of our unique  
8 Fe–NiCoP@C electrode in real HSAB applications. The power density of HSABs with  
9 different air electrodes was also investigated, as shown in Figure 6d. HSABs with the  
10 Fe–NiCoP@C air electrode obtained the highest power density of 621 mW g<sup>-1</sup>  
11 compared with those with Fe–NiCoP (532 mW g<sup>-1</sup>) and NiCoP (473 mW g<sup>-1</sup>), thereby  
12 indicating the excellent ORR performance of the Fe–NiCoP@C air electrode. The  
13 capacities of the batteries were also investigated, as shown in Fig. S17. The battery with  
14 1 M Na-BP-TEGDME displayed a capacity of around 15 Ah L<sup>-1</sup>, which is comparable  
15 with the recently reported Na-aqueous-catholyte redox flow battery (17.3 Ah L<sup>-1</sup>) [54].  
16

#### 17 **4. Conclusion**

18 In summary, we demonstrate a strategy to prepare binder-free 3D microflowers  
19 morphology of the Fe–NiCoP@C catalyst on the nickel foam as a highly efficient  
20 bifunctional air cathode for HSABs. The carbon layer effectively stabilizes the Fe–  
21 NiCoP electrolyte interface and improves the electron conduction and electrochemical  
22 activity. The DFT calculations reveal that the Fe dopant not only facilitates the electrical

1 property of Fe–NiCoP but also performs as the active site for ORR/OER and reduces  
2 the free energies of adsorption of the oxygen-containing intermediates, thus leading to  
3 improved ORR and OER kinetics. This study sheds new light into the design and  
4 improvement of TMPs catalysts for ORR/OER and the new understanding can be  
5 applied to other fields in electrocatalysis.

6

#### 7 **CRedit authorship contribution statement**

8 **Yao Kang:** Methodology, Investigation, Data curation, Writing-Original draft  
9 preparation. **Shuo Wang:** DFT calculation, DFT Writing-Reviewing and Editing. **Siqi**  
10 **Zhu:** Data curation. **Haixing Gao:** Writing-review & editing. **Kwan San Hui:** Writing-  
11 review & editing. **Feng Bin:** Verification. **Xi-Lin Wu:** TEM investigation supporting.  
12 **Wenjie Mai:** Writing-review & editing. **Ling Zhu:** Writing-review & editing. **Feng**  
13 **Liang:** Supervision, Funding acquisition, Conceptualization, Writing Reviewing and  
14 Editing. **Fuming Chen:** Electrocatalytic analysis, Writing-review & editing. **Kwun**  
15 **Nam Hui:** Supervision, Funding acquisition, Writing-Reviewing and Editing.

16

17 **Acknowledgement:** This work was funded by the Science and Technology  
18 Development Fund, Macau SAR (File no. 0191/2017/A3, 0041/2019/A1,  
19 0046/2019/AFJ, 0021/2019/AIR), University of Macau (File no. MYRG2017-00216-  
20 FST and MYRG2018-00192-IAPME), the UEA funding, Zhejiang Province Basic  
21 Public Welfare Research Project (LGF19B070006), Science and Technology Program  
22 of Guangzhou (2019050001), National Key Research and Development Program of



1 China (2019YFE0198000), Education Department of Guangdong Province  
2 (2019KZDXM014). F. Chen acknowledges the Pearl River Talent Program  
3 (2019QN01L951). The DFT calculations were performed at High Performance  
4 Computing Cluster (HPCC) of Information and Communication Technology Office  
5 (ICTO) at University of Macau.

6

### 7 **Declaration of Competing Interest**

8 There are no conflicts to declare.

9

### 10 **Appendix A. Supplementary data**

11 Supplementary material related to this article can be found, in the online version.

12

### 13 **Reference**

- 14 [1] Y. Kang, S. Wang, Y. Liu, K.S. Hui, H. Li, K.W. Ng, F. Liang, J. Geng, X. Hong, W.  
15 Zhou, K.N. Hui, Unveiling the Origin of Catalytic Sites of Pt Nanoparticles Decorated  
16 on Oxygen-Deficient Vanadium-Doped Cobalt Hydroxide Nanosheet for Hybrid  
17 Sodium–Air Batteries, *ACS Applied Energy Materials*, 3 (2020) 7464-7473.
- 18 [2] Y. Kang, F. Liang, K. Hayashi, Hybrid Sodium–Air Cell with Na[FSA–  
19 C2C1im][FSA] Ionic Liquid Electrolyte, *Electrochimica Acta*, 218 (2016) 119-124.
- 20 [3] F. Liang, X. Qiu, Q. Zhang, Y. Kang, A. Koo, K. Hayashi, K. Chen, D. Xue, K.N.  
21 Hui, H. Yadegari, X. Sun, A liquid anode for rechargeable sodium-air batteries with low  
22 voltage gap and high safety, *Nano Energy*, 49 (2018) 574-579.

- 1 [4] X. Lin, Q. Sun, K. Doyle Davis, R. Li, X. Sun, The application of carbon materials  
2 in nonaqueous Na-O<sub>2</sub> batteries, *Carbon Energy*, 1 (2019) 141-164.
- 3 [5] H. Yadegari, X. Sun, Sodium–Oxygen Batteries: Recent Developments and  
4 Remaining Challenges, *Trends in Chemistry*, 2 (2020) 241-253.
- 5 [6] Y. Kang, S. Wang, K. San Hui, H.-F. Li, F. Liang, X.-L. Wu, Q. Zhang, W. Zhou, L.  
6 Chen, F. Chen, K.N. Hui, [Fe(CN)<sub>6</sub>] Vacancy-boosting Oxygen Evolution Activity of  
7 Co-based Prussian Blue Analogues for Hybrid Sodium-air Battery, *Materials Today*  
8 *Energy*, (2020) 100572.
- 9 [7] B. Cai, R. Hübner, K. Sasaki, Y. Zhang, D. Su, C. Ziegler, M.B. Vukmirovic, B.  
10 Rellinghaus, R.R. Adzic, A. Eychmüller, Core–Shell Structuring of Pure Metallic  
11 Aerogels towards Highly Efficient Platinum Utilization for the Oxygen Reduction  
12 Reaction, *Angewandte Chemie International Edition*, 57 (2018) 2963-2966.
- 13 [8] J. Li, Z. Xi, Y.-T. Pan, J.S. Spendelow, P.N. Duchesne, D. Su, Q. Li, C. Yu, Z. Yin,  
14 B. Shen, Y.S. Kim, P. Zhang, S. Sun, Fe Stabilization by Intermetallic L10-FePt and Pt  
15 Catalysis Enhancement in L10-FePt/Pt Nanoparticles for Efficient Oxygen Reduction  
16 Reaction in Fuel Cells, *Journal of the American Chemical Society*, 140 (2018) 2926-  
17 2932.
- 18 [9] Y. Guo, P. Yuan, J. Zhang, H. Xia, F. Cheng, M. Zhou, J. Li, Y. Qiao, S. Mu, Q. Xu,  
19 Co<sub>2</sub>P–CoN Double Active Centers Confined in N-Doped Carbon Nanotube:  
20 Heterostructural Engineering for Trifunctional Catalysis toward HER, ORR, OER, and  
21 Zn–Air Batteries Driven Water Splitting, *Advanced Functional Materials*, 28 (2018)  
22 1805641.

- 1 [10] M. Song, Y. He, M. Zhang, X. Zheng, Y. Wang, J. Zhang, X. Han, C. Zhong, W.  
2 Hu, Y. Deng, Controllable synthesis of Co<sub>2</sub>P nanorods as high-efficiency bifunctional  
3 electrocatalyst for overall water splitting, *Journal of Power Sources*, 402 (2018) 345-  
4 352.
- 5 [11] T. Liu, P. Li, N. Yao, G. Cheng, S. Chen, W. Luo, Y. Yin, CoP-doped MOF-based  
6 electrocatalyst for pH-universal hydrogen evolution reaction, *Angewandte Chemie*, 131  
7 (2019) 4727-4732.
- 8 [12] Y. Li, H. Zhang, M. Jiang, Q. Zhang, P. He, X. Sun, 3D Self-Supported Fe-Doped  
9 Ni<sub>2</sub>P Nanosheet Arrays as Bifunctional Catalysts for Overall Water Splitting, *Advanced*  
10 *Functional Materials*, 27 (2017) 1702513.
- 11 [13] Y. Jiang, Y. Lu, J. Lin, X. Wang, Z. Shen, A Hierarchical MoP Nanoflake Array  
12 Supported on Ni Foam: A Bifunctional Electrocatalyst for Overall Water Splitting,  
13 *Small Methods*, 2 (2018) 1700369.
- 14 [14] X. Zhang, X. Yu, L. Zhang, F. Zhou, Y. Liang, R. Wang, Molybdenum  
15 Phosphide/Carbon Nanotube Hybrids as pH-Universal Electrocatalysts for Hydrogen  
16 Evolution Reaction, *Advanced Functional Materials*, 28 (2018) 1706523.
- 17 [15] S. Surendran, S. Shanmugapriya, A. Sivanantham, S. Shanmugam, R. Kalai Selvan,  
18 Electrospun Carbon Nanofibers Encapsulated with NiCoP: A Multifunctional Electrode  
19 for Supercapattery and Oxygen Reduction, Oxygen Evolution, and Hydrogen Evolution  
20 Reactions, *Advanced Energy Materials*, 8 (2018) 1800555.
- 21 [16] H. Zhang, X. Li, A. Hähnel, V. Naumann, C. Lin, S. Azimi, S.L. Schweizer, A.W.  
22 Maijenburg, R.B. Wehrspohn, Bifunctional Heterostructure Assembly of NiFe LDH

- 1 Nanosheets on NiCoP Nanowires for Highly Efficient and Stable Overall Water  
2 Splitting, *Advanced Functional Materials*, 28 (2018) 1706847.
- 3 [17] C. Liu, G. Zhang, L. Yu, J. Qu, H. Liu, Oxygen Doping to Optimize Atomic  
4 Hydrogen Binding Energy on NiCoP for Highly Efficient Hydrogen Evolution, *Small*,  
5 14 (2018) 1800421.
- 6 [18] M. Kong, Z. Wang, W. Wang, M. Ma, D. Liu, S. Hao, R. Kong, G. Du, A.M. Asiri,  
7 Y. Yao, X. Sun, NiCoP Nanoarray: A Superior Pseudocapacitor Electrode with High  
8 Areal Capacitance, *Chemistry – A European Journal*, 23 (2017) 4435-4441.
- 9 [19] Y. Sun, L. Yuan, Z. Liu, Q. Wang, K. Huang, S. Feng, Optimization of oxygen  
10 evolution dynamics on RuO<sub>2</sub> via controlling of spontaneous dissociation equilibrium,  
11 *Materials Chemistry Frontiers*, 3 (2019) 1779-1785.
- 12 [20] M. Hou, F. Liang, K. Chen, Y. Dai, D. Xue, Challenges and perspectives of  
13 NASICON-type solid electrolytes for all-solid-state lithium batteries, *Nanotechnology*,  
14 31 (2020) 132003.
- 15 [21] C. Xu, K. Zhang, D. Zhang, S. Chang, F. Liang, P. Yan, Y. Yao, T. Qu, J. Zhan, W.  
16 Ma, B. Yang, Y. Dai, X. Sun, Reversible hybrid sodium-CO<sub>2</sub> batteries with low  
17 charging voltage and long-life, *Nano Energy*, 68 (2020) 104318.
- 18 [22] S. Grimme, Semiempirical GGA-type density functional constructed with a long-  
19 range dispersion correction, *Journal of Computational Chemistry*, 27 (2006) 1787-1799.
- 20 [23] G. Kresse, J. Furthmuller, Efficient iterative schemes for ab initio total-energy  
21 calculations using a plane-wave basis set, *Physical Review B*, 54 (1996) 11169-11186.
- 22 [24] J.P. Perdew, K. Burke, M. Ernzerhof, Generalized Gradient Approximation Made

- 1 Simple, Physical Review Letters, 77 (1996) 3865-3868.
- 2 [25] J.P. Perdew, Y. Wang, Pair-distribution function and its coupling-constant average  
3 for the spin-polarized electron gas, Phys Rev B, 46 (1992) 12947-12954.
- 4 [26] P.E. Blöchl, Projector augmented-wave method, Phys Rev B, 50 (1994) 17953-  
5 17979.
- 6 [27] H.J. Monkhorst, J.D. Pack, Special points for Brillouin-zone integrations, Phys  
7 Rev B, 13 (1976) 5188-5192.
- 8 [28] S. Grimme, J. Antony, S. Ehrlich, H. Krieg, A consistent and accurate ab initio  
9 parametrization of density functional dispersion correction (DFT-D) for the 94 elements  
10 H-Pu, The Journal of Chemical Physics, 132 (2010) 154104.
- 11 [29] S. Grimme, S. Ehrlich, L. Goerigk, Effect of the Damping Function in Dispersion  
12 Corrected Density Functional Theory, Journal of Computational Chemistry, 32 (2011)  
13 1456-1465.
- 14 [30] Q. Yang, T. Li, Z. Lu, X. Sun, J. Liu, Hierarchical construction of an ultrathin  
15 layered double hydroxide nanoarray for highly-efficient oxygen evolution reaction,  
16 Nanoscale, 6 (2014) 11789-11794.
- 17 [31] P. Xiao, W. Chen, X. Wang, A Review of Phosphide-Based Materials for  
18 Electrocatalytic Hydrogen Evolution, Advanced Energy Materials, 5 (2015) 1500985.
- 19 [32] C. Xuan, J. Wang, W. Xia, Z. Peng, Z. Wu, W. Lei, K. Xia, H.L. Xin, D. Wang,  
20 Porous Structured Ni-Fe-P Nanocubes Derived from a Prussian Blue Analogue as an  
21 Electrocatalyst for Efficient Overall Water Splitting, ACS Applied Materials &  
22 Interfaces, 9 (2017) 26134-26142.

- 1 [33] B. Zhang, Y.H. Lui, A.P.S. Gaur, B. Chen, X. Tang, Z. Qi, S. Hu, Hierarchical  
2 FeNiP@Ultrathin Carbon Nanoflakes as Alkaline Oxygen Evolution and Acidic  
3 Hydrogen Evolution Catalyst for Efficient Water Electrolysis and Organic  
4 Decomposition, *ACS Applied Materials & Interfaces*, 10 (2018) 8739-8748.
- 5 [34] Q. Zhang, D. Yan, Z. Nie, X. Qiu, S. Wang, J. Yuan, D. Su, G. Wang, Z. Wu, Iron-  
6 Doped NiCoP Porous Nanosheet Arrays as a Highly Efficient Electrocatalyst for  
7 Oxygen Evolution Reaction, *ACS Applied Energy Materials*, 1 (2018) 571-579.
- 8 [35] T. Zhai, L. Wan, S. Sun, Q. Chen, J. Sun, Q. Xia, H. Xia, Phosphate Ion  
9 Functionalized Co<sub>3</sub>O<sub>4</sub> Ultrathin Nanosheets with Greatly Improved Surface Reactivity  
10 for High Performance Pseudocapacitors, *Advanced Materials*, 29 (2017) 1604167.
- 11 [36] Y. Wu, X. Tao, Y. Qing, H. Xu, F. Yang, S. Luo, C. Tian, M. Liu, X. Lu, Cr-Doped  
12 FeNi-P Nanoparticles Encapsulated into N-Doped Carbon Nanotube as a Robust  
13 Bifunctional Catalyst for Efficient Overall Water Splitting, *Advanced Materials*, 31  
14 (2019) 1900178.
- 15 [37] V.H. Hoa, D.T. Tran, H.T. Le, N.H. Kim, J.H. Lee, Hierarchically porous nickel-  
16 cobalt phosphide nanoneedle arrays loaded micro-carbon spheres as an advanced  
17 electrocatalyst for overall water splitting application, *Applied Catalysis B:  
18 Environmental*, 253 (2019) 235-245.
- 19 [38] T. Wu, S. Sun, J. Song, S. Xi, Y. Du, B. Chen, W.A. Sasangka, H. Liao, C.L. Gan,  
20 G.G. Scherer, L. Zeng, H. Wang, H. Li, A. Grimaud, Z.J. Xu, Iron-facilitated dynamic  
21 active-site generation on spinel CoAl<sub>2</sub>O<sub>4</sub> with self-termination of surface  
22 reconstruction for water oxidation, *Nature Catalysis*, 2 (2019) 763-772.

- 1 [39] G. Zhang, B. Wang, J. Bi, D. Fang, S. Yang, Constructing ultrathin CoP  
2 nanomeshes by Er-doping for highly efficient bifunctional electrocatalysts for overall  
3 water splitting, *Journal of Materials Chemistry A*, 7 (2019) 5769-5778.
- 4 [40] Y. Li, B. Jia, B. Chen, Q. Liu, M. Cai, Z. Xue, Y. Fan, H.-P. Wang, C.-Y. Su, G. Li,  
5 MOF-derived Mn doped porous CoP nanosheets as efficient and stable bifunctional  
6 electrocatalysts for water splitting, *Dalton T*, 47 (2018) 14679-14685.
- 7 [41] H. Li, Q. Li, P. Wen, T.B. Williams, S. Adhikari, C. Dun, C. Lu, D. Itanze, L. Jiang,  
8 D.L. Carroll, G.L. Donati, P.M. Lundin, Y. Qiu, S.M. Geyer, Colloidal Cobalt  
9 Phosphide Nanocrystals as Trifunctional Electrocatalysts for Overall Water Splitting  
10 Powered by a Zinc–Air Battery, *Advanced Materials*, 30 (2018) 1705796.
- 11 [42] Z. Xiao, Y. Wang, Y.-C. Huang, Z. Wei, C.-L. Dong, J. Ma, S. Shen, Y. Li, S. Wang,  
12 Filling the oxygen vacancies in Co<sub>3</sub>O<sub>4</sub> with phosphorus: an ultra-efficient  
13 electrocatalyst for overall water splitting, *Energy & Environmental Science*, 10 (2017)  
14 2563-2569.
- 15 [43] S.T. Senthilkumar, S.O. Park, J. Kim, S.M. Hwang, S.K. Kwak, Y. Kim, Seawater  
16 battery performance enhancement enabled by a defect/edge-rich, oxygen self-doped  
17 porous carbon electrocatalyst, *Journal of Materials Chemistry A*, 5 (2017) 14174-14181.
- 18 [44] D. Yan, Y. Li, J. Huo, R. Chen, L. Dai, S. Wang, Defect Chemistry of Nonprecious-  
19 Metal Electrocatalysts for Oxygen Reactions, *Advanced Materials*, 29 (2017) 1606459.
- 20 [45] S. Chen, J. Duan, M. Jaroniec, S.-Z. Qiao, Nitrogen and Oxygen Dual-Doped  
21 Carbon Hydrogel Film as a Substrate-Free Electrode for Highly Efficient Oxygen  
22 Evolution Reaction, *Advanced Materials*, 26 (2014) 2925-2930.

- 1 [46] Y. Zhai, Z. Zhu, S. Dong, Carbon-based nanostructures for advanced catalysis,  
2 Chemcatchem, 7 (2015) 2806-2815.
- 3 [47] P. Wang, Z. Pu, Y. Li, L. Wu, Z. Tu, M. Jiang, Z. Kou, I.S. Amiin, S. Mu, Iron-  
4 Doped Nickel Phosphide Nanosheet Arrays: An Efficient Bifunctional Electrocatalyst  
5 for Water Splitting, ACS Applied Materials & Interfaces, 9 (2017) 26001-26007.
- 6 [48] L. Cai, B. Qiu, Z. Lin, Y. Wang, S. Ma, M. Wang, Y.H. Tsang, Y. Chai, Active site  
7 engineering of Fe- and Ni-sites for highly efficient electrochemical overall water  
8 splitting, Journal of Materials Chemistry A, 6 (2018) 21445-21451.
- 9 [49] A. Grimaud, K.J. May, C.E. Carlton, Y.-L. Lee, M. Risch, W.T. Hong, J. Zhou, Y.  
10 Shao-Horn, Double perovskites as a family of highly active catalysts for oxygen  
11 evolution in alkaline solution, Nature Communications, 4 (2013) 2439.
- 12 [50] Y. Tian, S. Wang, E. Velasco, Y. Yang, L. Cao, L. Zhang, X. Li, Y. Lin, Q. Zhang,  
13 L. Chen, A Co-Doped Nanorod-like RuO<sub>2</sub> Electrocatalyst with Abundant Oxygen  
14 Vacancies for Acidic Water Oxidation, iScience, 23 (2020) 100756.
- 15 [51] F. Ando, T. Tanabe, T. Gunji, S. Kaneko, T. Takeda, T. Ohsaka, F. Matsumoto,  
16 Effect of the d-Band Center on the Oxygen Reduction Reaction Activity of  
17 Electrochemically Dealloyed Ordered Intermetallic Platinum–Lead (PtPb)  
18 Nanoparticles Supported on TiO<sub>2</sub>-Deposited Cup-Stacked Carbon Nanotubes, ACS  
19 Applied Nano Materials, 1 (2018) 2844-2850.
- 20 [52] F.H.B. Lima, J. Zhang, M.H. Shao, K. Sasaki, M.B. Vukmirovic, E.A. Ticianelli,  
21 R.R. Adzic, Catalytic Activity–d-Band Center Correlation for the O<sub>2</sub> Reduction  
22 Reaction on Platinum in Alkaline Solutions, The Journal of Physical Chemistry C, 111



1 (2007) 404-410.

2 [53] X. Tian, X. Zhao, Y.-Q. Su, L. Wang, H. Wang, D. Dang, B. Chi, H. Liu, E.J.M.

3 Hensen, X.W. Lou, B.Y. Xia, Engineering bunched Pt-Ni alloy nanocages for efficient

4 oxygen reduction in practical fuel cells, *Science*, 366 (2019) 850.

5 [54] S.T. Senthilkumar, J. Han, J. Park, S. Min Hwang, D. Jeon, Y. Kim, *Energy*

6 efficient Na-aqueous-catholyte redox flow battery, *Energy Storage Mater*, 12 (2018)

7 324-330.

8